ACS OMEGA

http://pubs.acs.org/journal/acsodf

Article

Synthesis, Structure, and Properties of Complexes Based on 2,4-Bis-(triazol-1-yl)benzoic Acid as a Ligand

Yunxia Yang,* Yingwa Guo, Shiying Xia, Xiaona Ma, and Xiangxiang Wu*

Cite This: *ACS Omega* 2022, 7, 18276−18291

Read Online

ACCESS | Metrics & More | Article Recommendations | Supporting Information

ABSTRACT: Using 2,4-bis-(triazol-1-yl)-benzoic acid as the main ligand and terephthalic acid (TPA) as the auxiliary ligand, combined with $Cd(NO_3)_2{\cdot}4H_2O$ and $Zn(NO_3)_2{\cdot}6H_2O$, self-assembly under solvothermal conditions gave three novel complexes: $[Cd_{0.5}(L)(H_2O)]$ (**1**), $[Cd(L)(TPA)_{0.5}(H_2O)]{\cdot}H_2O$ (**2**), and $[Zn(L)(TPA)_{0.5}]{\cdot}H_2O$ (**3**) (TPA = terephthalic acid). The crystal structure test showed that complex **1** belongs to the triclinic crystal system and the $P\bar{1}$ space group and complexes **2** and **3** belong to the monoclinic crystal system and the $P2_1/c$ space group. Solid-state fluorescence experiments show that complexes **1**, **2**, and **3** all have excellent optical properties: among them, complexes **1** and **3** can selectively detect MnO_4^- with low detection limits (0.96 μM and 0.232 μM, respectively) and complex **2** can detect $Cr_2O_7^{2-}$ [limit of detection (LOD) = 0.035 μM], and the most interesting thing is that all three complexes can be used as sensors for detecting Fe^{3+} (LOD = 0.76 μM, 0.657 μM, and 0.11 μM, respectively). In addition, the detection capabilities of these three complexes for different amino acids and antibiotics were also analyzed, and the results showed that all three complexes can effectively detect tetracycline hydrochloride through the quenching effect and **2** and **3** can selectively detect tryptophan via the fluorescence enhancement effect.

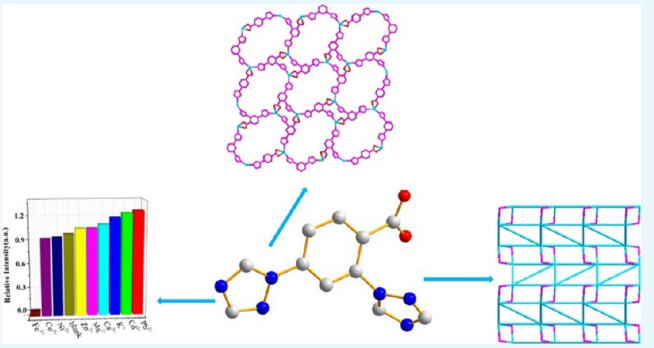

1. INTRODUCTION

Metal organic framework (MOF) compounds can be referred to as complexes (CPs), which are porous materials with a network structure formed via self-assembly of metal ions that provide empty orbitals and organic ligands that provide lone pairs of electrons.[1,2] By rationally selecting metal ions and multifunctional organic ligands, complexes with specific pore sizes, novel structures, and unique properties can be synthesized. In addition, the properties of the complexes can be further regulated through strategies such as "post-synthesis" modification. At present, complex materials are widely used in sensors,[3] gas storage[4] and separation, heterogeneous catalysis,[5,6] drug delivery,[7] magnetism, and so on.[8,9] In recent years, a large number of literature studies have reported that various complexes have been successfully used as luminescence sensors and have shown good selectivity and sensitivity for the detection of anions, cations, explosives, small molecules, antibiotics, amino acids, and other substances.[10−15] However, how to control the synthesis of complexes that meet the requirements of specific luminescence sensors is still a huge challenge for chemists. For complexes, rational selection of metal centers and predesigned functional organic ligands are important prerequisites for their fluorescence properties. As we all know, Zn^{2+}, Cd^{2+}, and Ln^{3+} are usually used as luminescent cations, and the introduction of functional organic ligands with guest accessible sites on the pore surface has proven to be a simple and effective strategy, which can improve the recognition ability of molecules with noncoordinating functional groups or unsaturated open metal sites.

In addition, the mixed ligand has a flexible and diverse coordination environment, which can provide a rigid and stable structure for the construction of MOFs. More importantly, the use of high-π coupling ligands and hybrid assembly strategies can enable MOFs to exhibit unique luminescence properties. For example, triazole-carboxylic acid organic ligands contain both N donors and O donors and exhibit flexible and diverse coordination modes, and by adjusting the ratio of organic ligands to metal ions, MOFs of different dimensions can be obtained.[16] Among them, there are Co-MOFs synthesized by adjusting pH and using transition metals that have the ability to adsorb methyl orange (MO), and there are also MOFs synthesized with noble metals such as Ag, W, V, and so on that can adsorb cationic dyes.[17] The bifunctional organic ligand 2,4-bis-(triazol-1-yl)benzene car-

Received: December 29, 2021
Accepted: May 12, 2022
Published: May 24, 2022

https://doi.org/10.1021/acsomega.1c07351
ACS Omega 2022, 7, 18276−18291

Table 1. Crystallographic Parameters of Complexes 1−3

complex	1	2	3
CCDC	2167053	2167054	2167055
formula	$C_{64}H_{54}Cd_2N_{12}O_4$	$C_{15}H_{11}CdN_6O_5$	$C_{15}H_9N_6O_4Zn$
formula weight	1279.99	467.70	402.65
crystal color	yellow	colorless	colorless
crystal shape	needle	block	block
crystal system	triclinic	monoclinic	monoclinic
space group	$P\bar{1}$	P21/c	$P2_1/c$
a/Å	7.4247 (5)	11.07497 (17)	9.36351 (10)
b/Å	12.1365 (7)	20.3666 (3)	16.86500 (16)
c/Å	26.4282 (17)	7.17100 (11)	9.42877 (10)
β/°	90	91.8258 (14)	103.5753 (11)
V/Å3	2381.4 (3)	1616.66 (4)	1447.35 (3)
Z, D_{calc} ($Mg{\cdot}m^{-3}$)	2, 1.785	4, 1.922	4, 1.848
μ/mm−1	0.97	11.24	2.74
θ range for data collection	2.7−50.6	4.0−76.2°	2.8−49.2
limiting indices	$-16 \le h \le 16$	$-13 \le h \le 13$	$-11 \le h \le 11$
	$-26 \le k \le 22$	$-20 \le k \le 24$	$-21 \le k \le 20$
	$-57 \le l \le 47$	$-8 \le l \le 9$	$-11 \le l \le 8$
reflection number	87,693/46,186 [$R_{(int)}$ = 0.039]	10,661/3195 [$R_{(int)}$ = 0.026]	9178/2875 [$R_{(int)}$ = 0.021]
R_1,w$R2[I > 2\sigma(I)]$	0.064, 0.232	0.025, 0.064	0.028, 0.072
S	1.18	1.05	1.05

boxylic acid contains a large $\pi-\pi$ conjugated system, which combines the advantages of two functional groups, so it is worth our research.

Based on this guiding idea, three new complexes were obtained in this thesis via self-assembly under solvothermal conditions by using 2,4-di-(triazol-1-yl)-benzoic acid (HL) as the main ligand and terephthalic acid (TPA) as the auxiliary ligand and selecting transition metal ions with similar d^{10} structures as metal centers (Zn^{2+} and Cd^{2+}), and their corresponding properties were investigated.

2. EXPERIMENTAL SECTION

2.1. Reagents and Methods. See the Supporting Information for reagents and instruments used in the experiment.

2.2. Preparation of Complexes. *2.2.1. Preparation of $[Cd_{0.5}(L)(H_2O)]$ (1).* First, 0.0026 g (0.01 mmol) of organic ligand HL was dispersed in 6 mL of a solvent mixture of acetonitrile and water (v/v = 5:1), and then, $Cd(NO_3)_2{\cdot}4H_2O$ (0.25 mL, 0.04 mol L^{-1}) solution was added and stirred to form a suspension, which was transferred to a reaction vessel and heated at 125 °C for 96 h. After cooling to room temperature, colorless bulk crystals were obtained via centrifugation and washed with acetonitrile and distilled water. Finally, the solid was naturally dried in air to obtain complex **1** with a yield of 44.8% (based on Cd). FT-IR data: (KBr, cm^{-1}, Figure S1): 3448(sh), 2930(w), 1604(s), 1519(m), 1374(s), 1138(w), 665(s).

2.2.2. Preparation of $[Cd(L)(TPA)_{0.5}(H_2O)]{\cdot}H_2O$ (2). First, 0.0026 g (0.01 mmol) of organic ligand HL and 0.0033 g (0.02 mmol) of TPA were dispersed in 6 mL of a solvent mixture of acetonitrile and water (v/v = 5:1), and then, $Cd(NO_3)_2{\cdot}4H_2O$ (0.25 mL, 0.04 mol L^{-1}) solution was added to it and stirred to form a suspension, which was transferred to a reaction vessel and heated at 125 °C for 96 h. Colorless bulk crystals were obtained via centrifugation and washed with acetonitrile and distilled water. Finally, the solid was dried naturally in air to give complex **2** with a yield of 41.3% (based on Cd). FT-IR data: (KBr, cm^{-1}, Figure S1): 3415(br), 3144(w), 1607(s), 1565(vs), 1517(w), 1397(vs), 11283(m), 1205(w), 1133(m), 1049(w), 982(m), 845(m), 754(m), 658(m).

2.2.3. Preparation of $[Zn(L)(TPA)_{0.5}]{\cdot}H_2O$ (3). The preparation method and conditions of complex **3** were the same as those of complex **2**, except that metal salt $Cd(NO_3)_2{\cdot}4H_2O$ was replaced by $Zn(NO_3)_2{\cdot}4H_2O$, and colorless bulk crystals were obtained with a yield of 43.4% (based on Zn). FT-IR data: (KBr, cm^{-1}, Figure S1): 3447(sh), 2929(w), 1603(s), 1518(m), 1374(s), 1137(w), 665(s).

3. RESULTS AND DISCUSSION

3.1. Crystal Structure Description. *3.1.1. Crystal Structure of $[Cd_{0.5}(L)(H_2O)]$ (1).* Complex **1** crystallizes in the triclinic system of space group $P\bar{1}$ (Table 1). The asymmetric structural unit contains 0.5 cadmium ions, one ligand anion, and one coordinated water molecule. The Cd(II) ion is linked through ligand HL, showing a μ_2-η^0: η^0: η^1: η^0: η^1: η^0 coordination pattern (Figure 1a). As shown in Figure 1b, the cadmium ion is coordinated by four oxygens and two nitrogens, showing a six-coordinated octahedral geometry. Among them, the four oxygens come from two oxygens (O1 and O1i) on the main ligand and two oxygens (O1W and O1Wi) in the coordination water molecule, and the two nitrogens come from the ligand triazole ring (N2ii and N2iii)). HL ligands link adjacent Cd^{2+} to further form a one-dimensional chain (Figure 1c), and the distance between adjacent Cd1···Cd2 is 7.1137(4) Å. The one-dimensional chains are connected by ligands in different orientations to form a two-dimensional layered structure (Figure 1d,e).

3.1.2. Crystal Structure of $[Cd(L)(TPA)_{0.5}(H_2O)]{\cdot}H_2O$ (2). Complex **2** crystallizes in the monoclinic system of space group $P2_1/c$ and exhibits a three-dimensional framework structure. The asymmetric structural unit includes a metal cadmium ion, a main ligand anion, 0.5 terephthalate anion, a coordinating water molecule, and a guest water molecule. The HL ligand in complex **2** is fully deprotonated and has a μ_3-η^1: η^1: η^0: η^1: η^0: η^0 coordination pattern (Figure 2a). As shown in Figure 2b,

https://doi.org/10.1021/acsomega.1c07351
ACS Omega 2022, 7, 18276−18291

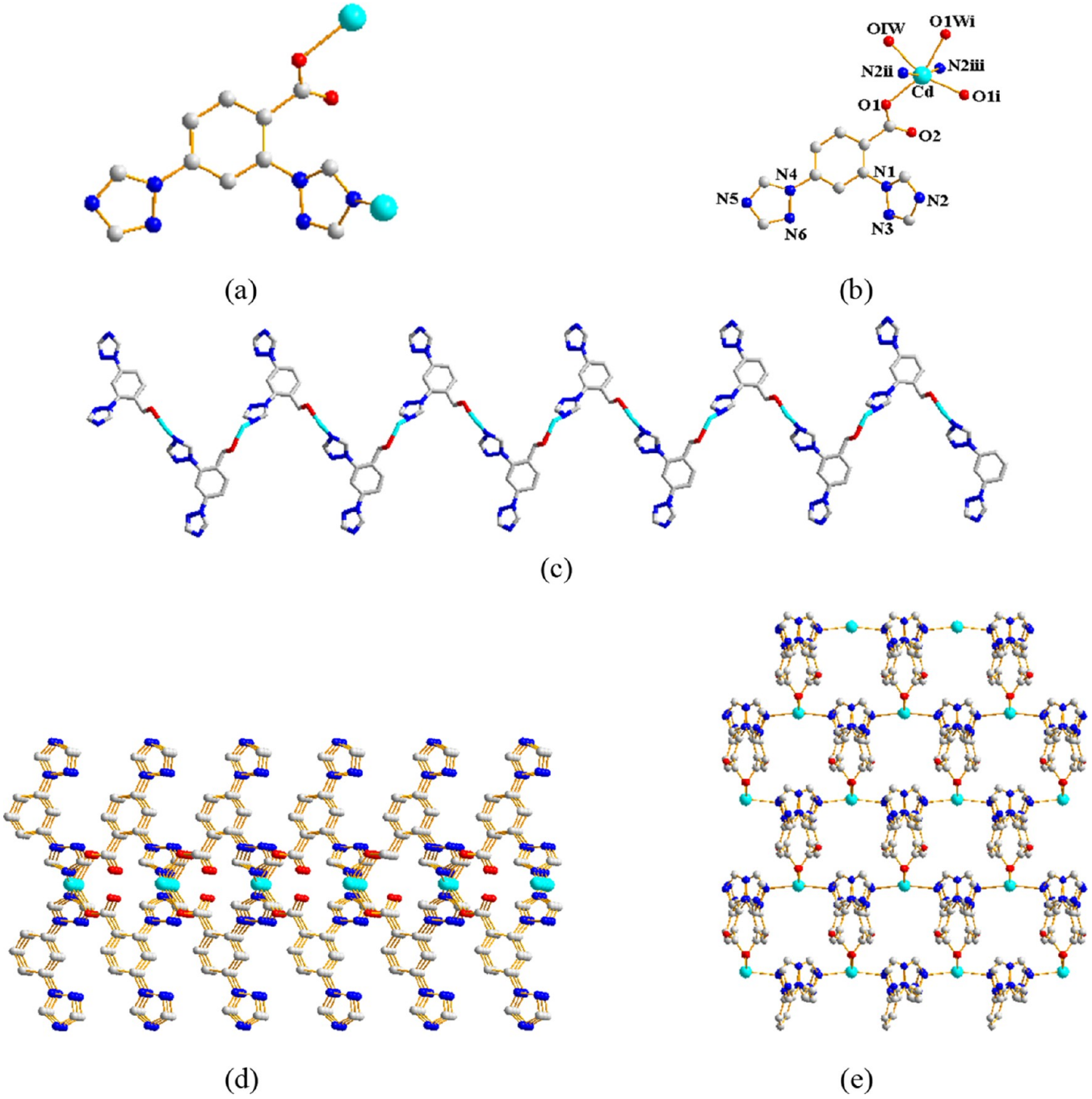

Figure 1. (a) Coordination pattern diagram of ligand HL and (b) coordination environment of complex **1** (all hydrogen atoms are deleted for clarity). Symmetric opcode: (i) $1 - x, y, 0.5 - z$; (ii) $0.5 - x, 0.5 + y, z$; and (iii) $0.5 + x, 0.5 + y, 0.5 - z$. (c) One-dimensional chain structure of complex **1**. (d) Two-dimensional laminar structure of complex **1** from the *a* axis and (e) two-dimensional laminar structure of complex **1** from the *c* axis.

the Cd^{2+} center is coordinated by five oxygens and two nitrogens, presenting a seven-coordinated pentagonal bipyramid spatial configuration. Among them, the five oxygen atoms come from two carboxylate oxygens (O1 and O2) on a main ligand, two carboxylate oxygens (O3 and O4) on TPA, and one of the coordinating water molecule oxygen (O5W), and the two nitrogen atoms from the ligand triazole ring (N3i and N6ii). HL ligands link adjacent Cd^{2+} to further form a one-dimensional chain (Figure 2c). Among them, the two Cd^{2+} ions are connected by ligands to form two different types of bimetallic structural units, where the minimum distance of Cd···Cd is 6.4044(5) Å and the maximum distance is 11.3557(4) Å (Figure 2d). Subsequently, these two different types of building blocks are sequentially connected by ligands to form a two-dimensional layered structure (Figure 2e). The layers are longitudinally connected by oxygen atoms on auxiliary ligands to form a three-dimensional framework (Figure 2f). Figure 2g shows the three-dimensional topology of complex **2**. According to TOPOS 4.0[18] software analysis, its topology symbol can be expressed as $\{4.8^2\}_2\{4.8^5\}_2\{8\}$.

*3.1.3. Crystal Structure of $[Zn(L)(TPA)_{0.5}]\cdot H_2O$ (**3**).* Complex **3** crystallizes in the monoclinic system of space group $P2_1/c$.

https://doi.org/10.1021/acsomega.1c07351
ACS Omega 2022, 7, 18276−18291

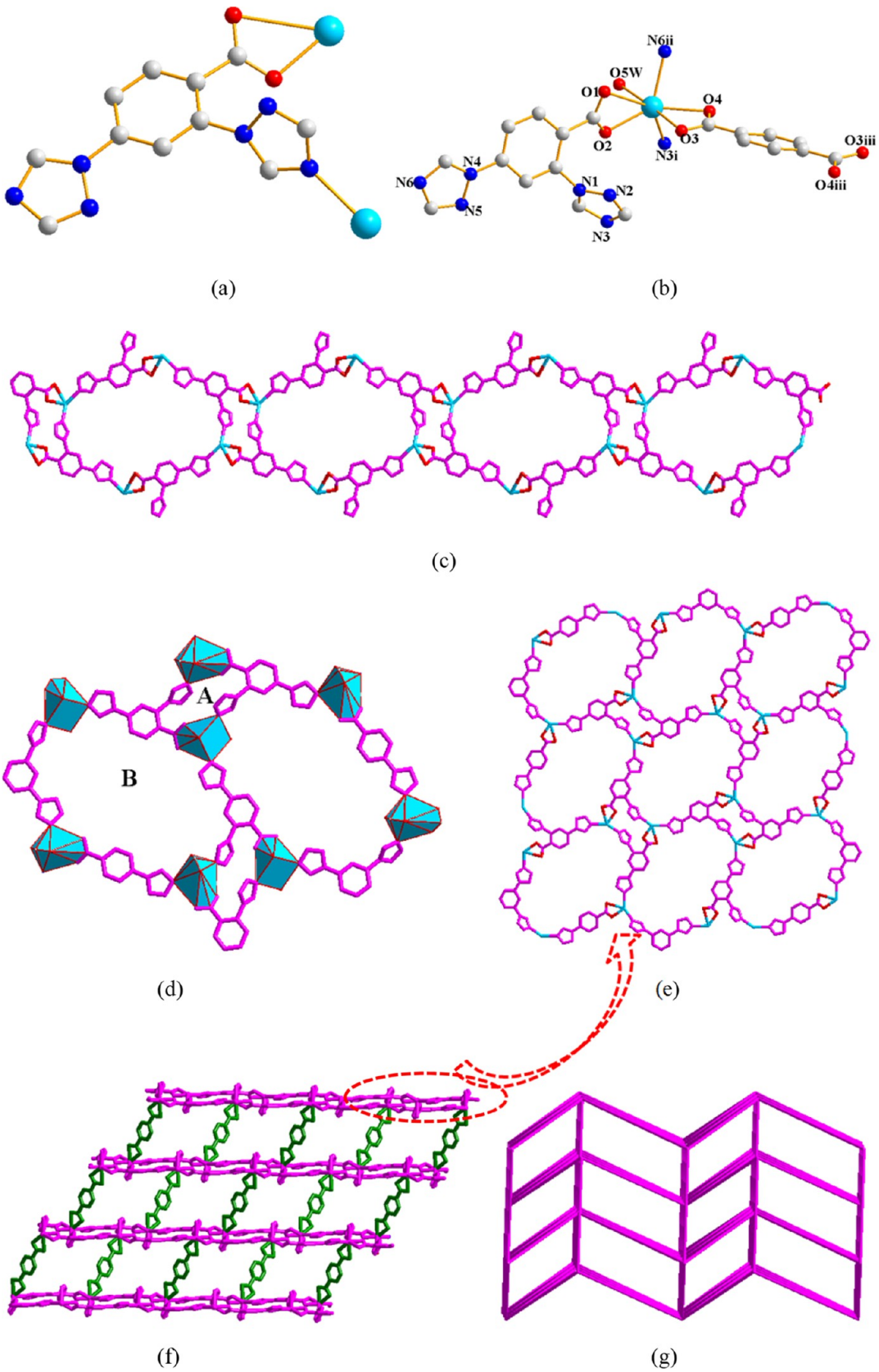

Figure 2. (a) Coordination pattern diagram of ligand HL; (b) map of the coordination environment of complex **2**; symmetric opcode: (i) $-x + 1$, $-y + 1$, $-z + 1$; (ii) $x + 1$, $-y + 1/2$, $z + 1/2$; (iii) $-x + 2$, $-y + 1$, $-z$; and (iv) $x - 1$, $-y + 1/2$, z; (c) one-dimensional chain of complex **2**; (d) two different types of unit structures in complex **2**; (e) two-dimensional laminar structure of complex **2**; (f) three-dimensional framework structure of complex **2**; and (g) three-dimensional topological structure of complex **2**.

https://doi.org/10.1021/acsomega.1c07351
ACS Omega 2022, 7, 18276−18291

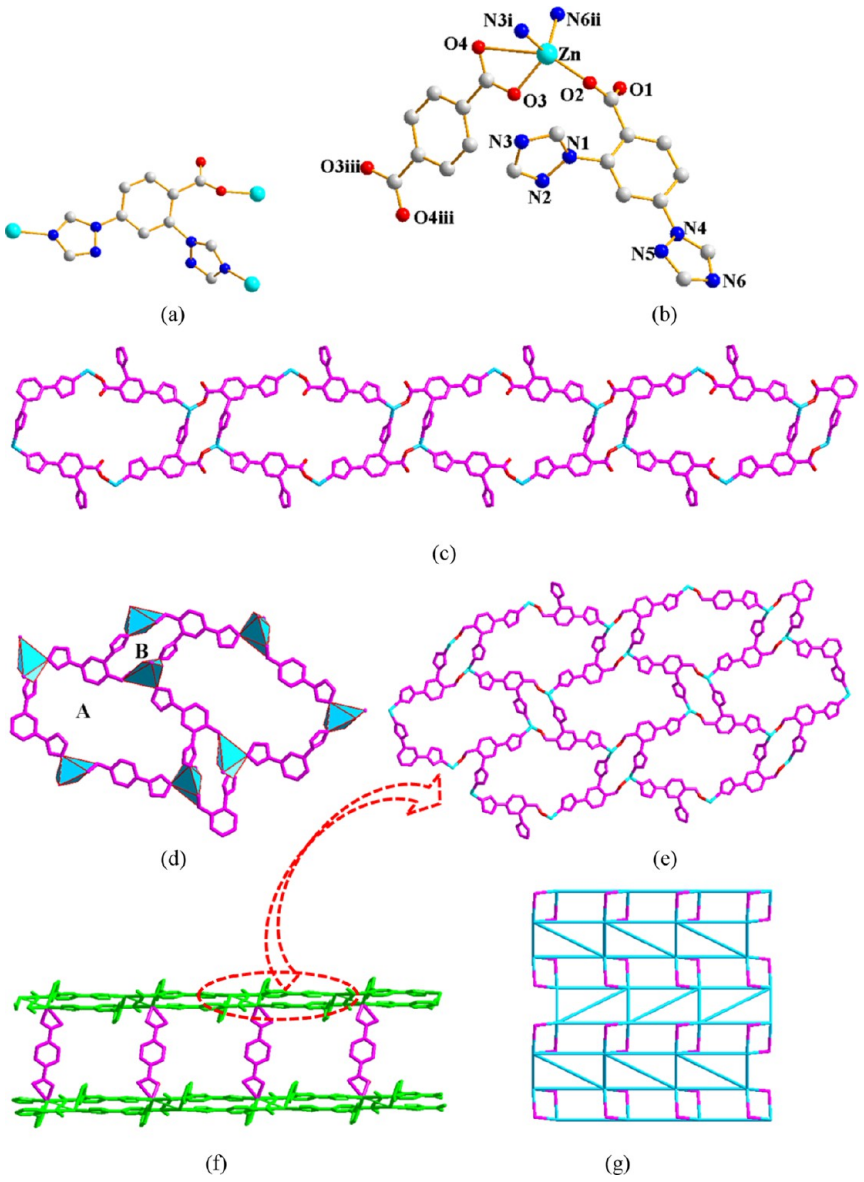

Figure 3. (a) Coordination pattern diagram of ligand HL; (b) map of the coordination environment of complex **3**; symmetric opcode: (i) $-x + 1$, $-y + 1$, $-z$; (ii) $x + 1$, $-y + 3/2$, $z - 1/2$; (iii) $-x + 2$, $-y + 1$, $-z + 1$; and (iv) $x - 1$, $-y + 3/2$, z; (c) one-dimensional chain of complex **3**; (d) two different types of unit structures in complex **3**; (e) two-dimensional laminar structure of complex **3**; (f) three-dimensional framework structure of complex **3**; and (g) three-dimensional topological structure of complex **3**.

The asymmetric unit includes a metallic zinc ion, a main ligand anion, 0.5 terephthalate anion, and a guest water molecule. The HL ligand in complex **3** is half-protonated and exhibits a μ_3-η^0: η^1: η^1: η^0: η^0: η^1 coordination pattern (Figure 3a). As shown in Figure 3b, Zn is coordinated by three oxygen atoms and two nitrogen atoms, showing a five-coordinated trigonal bipyramidal spatial configuration. Among them, the three oxygen atoms come from one carboxylate oxygen (O2) in a main ligand and two carboxylate oxygens (O3 and O4) on the TPA auxiliary ligand, and the two nitrogen atoms come from the ligand (N3i and N6ii) on the triazole ring. HL ligands link adjacent Zn^{2+} to further extend to form a one-dimensional chain (Figure 3c). Among them, two Zn^{2+} ions are connected by ligands in different directions to form two different types of bimetallic structural units (Figure 3d), where the minimum distance of Zn···Zn is 5.0766(4) Å and the maximum distance is 12.2756(4) Å. Subsequently, these two different types of building blocks are sequentially connected by ligands to form a two-dimensional layered structure (Figure 3e). The layers are connected by the carboxylic acid oxygen atoms on the auxiliary ligands to form a three-dimensional framework structure. Figure 3f,g shows the three-dimensional topological structure of complex **3**. According to TOPOS 4.0 software analysis, its topological symbol can be expressed as $\{4.8^2\}_2\{4.8^5\}_2\{8\}$.

3.2. Infrared Analysis of Complex 1−3. Figure S1 shows the infrared (IR) spectrum of complex **1**−**3**. For the HL ligand, the peak at 3441 cm^{-1} mainly corresponds to the stretching vibration peak of −OH in the carboxyl group of the ligand, the peak at 1711 cm^{-1} is mainly the stretching vibration peak of −C═O in the carboxyl group of the ligand, the peak at 1610 cm^{-1} is the stretching vibration peak of C═N on the imidazole ring, and the peak at 1517 cm^{-1} is the stretching vibration peak of C═C on the benzene ring. After the complexes are formed, the −C═O stretching vibration peak of

https://doi.org/10.1021/acsomega.1c07351
ACS Omega 2022, 7, 18276−18291

the ligand at 1711 cm^{-1} disappears, indicating that the carboxyl group in the ligand is coordinated with the metal ion. In addition, it is also observed that the stretching vibration peak of C═N in the ligand shifts from 1610 to 1566 cm^{-1} after the formation of the complex, indicating that the N in the ligand is also coordinated with the metal ion. In summary, the complexes were successfully prepared.

3.3. Powder X-ray Diffraction and Thermogravimetric Analysis of Complexes 1−3. In order to verify the phase purity of the synthesized complexes, the powder X-ray diffraction (PXRD) test was carried out in the 2θ range of 5−50°. By comparing the experimental data and the simulated data, it was found that the peak shapes of the two PXRD spectra were similar and the positions were consistent, which indicates that the synthesized complexes **1**−**3** have excellent phase purity (Figure S2).

Thermogravimetric analysis (TGA) of the complexes was performed at room temperature ~800 °C under a N_2 atmosphere to evaluate the thermal stability of the complexes. As shown in Figure S3, complex **1** shows a weight loss of 5.64% from room temperature to 240 °C, which is mainly due to the loss of coordination water molecules (the theoretical calculation value is 5.45%), and the skeleton begins to collapse obviously at 240 °C. Complex **2** shows a weight loss of 4.5% from room temperature to 99 °C, which is mainly due to the loss of coordinated water molecules (the theoretical calculation value is 3.8%), and then remains stable until the TGA curve drops sharply at 351 °C and the framework begins to collapse. Complex **3** shows a weight loss of 3.1% from room temperature to 208 °C, which is mainly due to the loss of guest water molecules (the theoretical calculation value is 4.4%), and then remains stable until the framework begins to decompose and collapse at 532 °C.

3.4. Solid-State Fluorescence Properties of Complexes 1−3. We have studied the solid-state luminescence properties of complexes **1**−**3** and HL at room temperature and found that the synthesized complexes have good fluorescence properties, so the fluorescence properties have been systematically studied. As shown in Figure 4, ligand HL has a maximum emission peak at 398 nm under the excitation wavelength of 316 nm, which may be caused by the $\pi^* \rightarrow \pi$ or $\pi^* \rightarrow$ n electronic transition inside the ligand.[19] The maximum emission wavelengths are λ_{em} = 406 nm (λ_{ex} = 319 nm) for complex **1**, λ_{em} = 406 nm (λ_{ex} = 310 nm) for complex **2**, and λ_{em} = 405 nm (λ_{ex} = 312 nm) for complex **3**. Compared with the maximum emission peak of the blank group, the maximum emission wavelength of the synthesized complex **2** shows a red shift, which may be caused by charge transfer between substances, mainly including charge transfer between ligands and metal ions, between metal ions and ligands, between ligands and ligands, and between metal ions and metal ions.

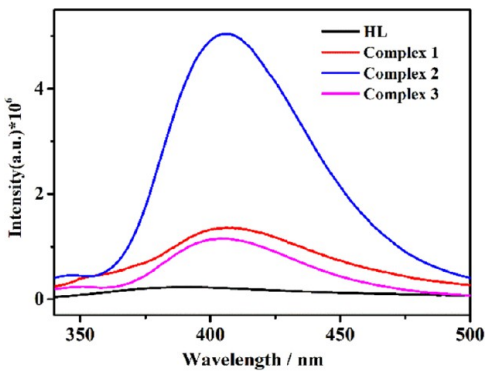

Figure 4. Solid-state fluorescence curves of ligand HL and complexes **1**−**3**.

3.4.1. Fluorescence Recognition of Different Organic Solvents by Complexes 1−3. Considering the excellent solid-state fluorescence properties of the complexes, we studied its fluorescence sensing ability in different organic solvents. 3 mg of the complex powder was weighed and dispersed into 4 mL of different common organic solvents [acetonitrile (CH_3CN), acetone (aectone), nitrobenzene (NB), water (H_2O), ethanol (EtOH), ethyl acetate (ethyl acetate), *N*,*N*-dimethylformamide (DMF), *N*-methylpyrrolidone (NMP), dimethyl sulfoxide (DMSO), dichloromethane (CH_2Cl_2), and chloroform ($CHCl_3$)]; the mixture was ultrasonicated for 20 min to make it evenly mixed; and then, its fluorescence response was tested. As shown in Figure 5, different organic solvents have different effects on the fluorescence intensity of complexes. Compared with the fluorescence intensity in the aqueous solution of the complexes, it is clearly observed that the acetonitrile solvent can enhance the fluorescence intensity of the three complexes. In addition, it can be observed that NB has a significant quenching effect on the fluorescence of complexes **2** and **3** and acetone has a significant quenching effect on the fluorescence of complex **1**, which may be due to the special interaction between the organic solvent molecules and the surface of the complexes.[20,21] This means that the synthesized complex can be used as a fluorescence sensor to selectively detect acetone molecules and NB.

3.4.2. Fluorescence Recognition of Cations by Complexes 1−3. To explore the fluorescence recognition ability of complexes **1**−**3** for cations, we carried out the following experiments. 2 mg of the well-ground complex was dispersed into 2 mL of distilled water; then, it was mixed with an equal volume of $M(NO_3)_X$ (M = Zn^{2+}, Cd^{2+}, Al^{3+}, Ni^{2+}, Mg^{2+}, Ag^+, Fe^{3+}, Pb^{2+}, Cu^{2+}, and Co^{2+}) solutions with a concentration of 1.0×10^{-3} mol·L^{-1} and ultrasonicated for 30 min to form a suspension; and finally its fluorescence change was tested. As shown in Figure 6, Fe^{3+} has an obvious fluorescence quenching effect on the three complexes, and the quenching rates are 92, 70.4, and 73%, respectively, while other metal cations have a small effect on the fluorescence intensity of the complexes, which shows that these three complexes can be used as fluorescent probes to selectively recognize Fe^{3+}, and it can be seen from the fluorescence spectrum that the complexes can recognize Fe^{3+} uniquely (Figure 6d−f) and the addition of other metal cations does not affect the selective detection of Fe^{3+} by complexes.

To evaluate the selectivity of the sensing system, the fluorescence responses of MOF and MOF@X (X = Fe^{3+}) complexes in the presence of different interfering substances were recorded. As shown in Figure 6g−i, Fe^{3+} (2 mL, 1.0×10^{-3} mol L^{-1}) can significantly quench the fluorescence of the corresponding complexes, while the fluorescence quenching effect of other metal ions on the complexes is not too obvious. In addition, it can be observed that the metal ions that may cause interference do not affect the "off" process of Fe^{3+}-induced complex fluorescence, which indicates that the complexes are more selective for the detection of Fe^{3+} than of other metal ions.

To evaluate the sensitivity of the "off" sensor, a concentration titration experiment was performed. As shown

https://doi.org/10.1021/acsomega.1c07351
ACS Omega 2022, 7, 18276−18291

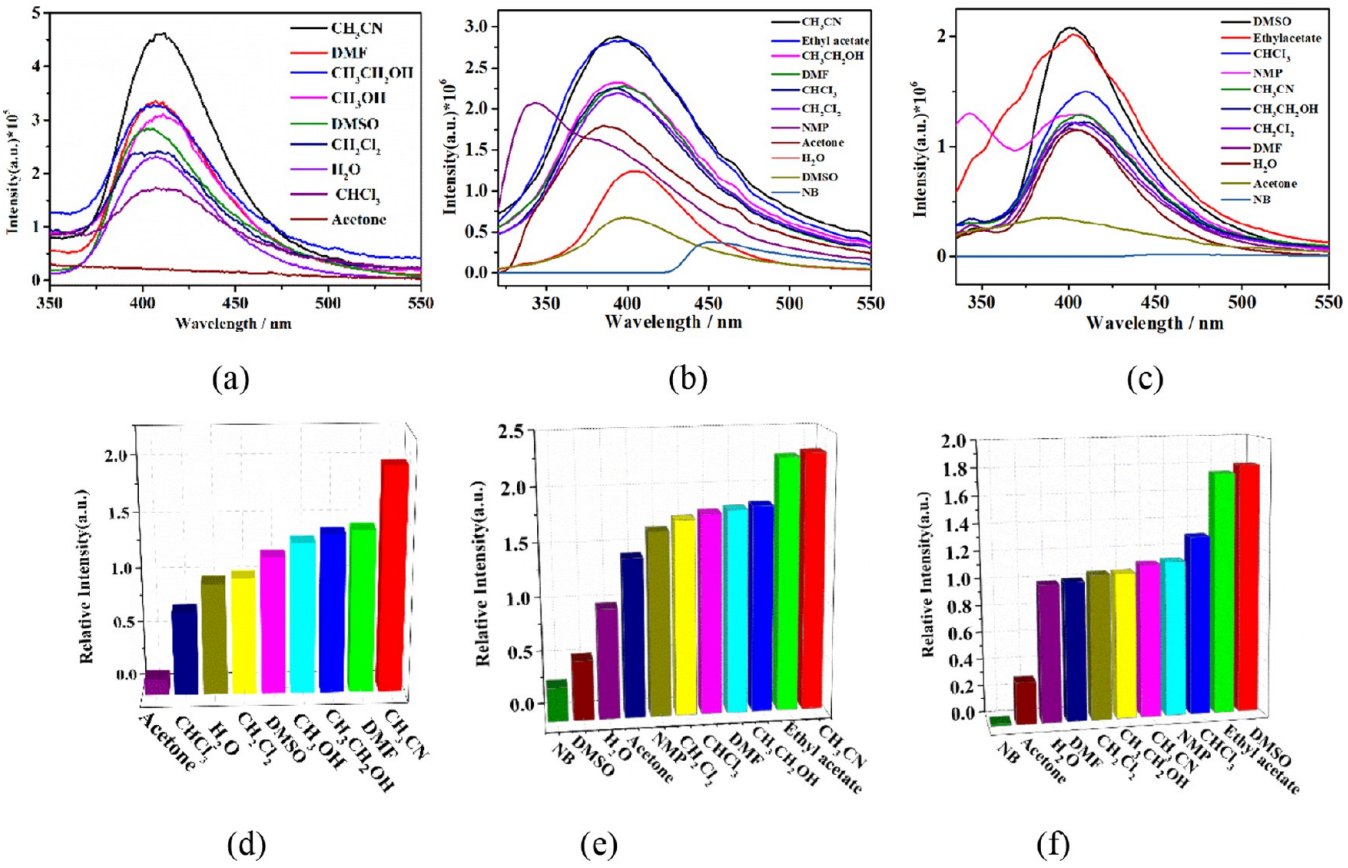

Figure 5. Fluorescence spectra of complexes after the addition of different analytes: (a) complex **1**; (b) complex **2**; and (c) complex **3**. Histogram of the relative fluorescence intensity of complexes in the presence of different analytes: (d) complex **1**; (e) complex **2**; and (f) complex **3**.

in Figure 7a–c, the fluorescence intensity of the corresponding complex suspensions decreased gradually with the increase of Fe^{3+} concentration. The fluorescence quenching efficiency can be quantitatively described by the Stern–Volmer (SV) equation: $I_0/I = 1 + K_{SV}[M]$,[22−25] where I_0 and I are the fluorescence intensities of the complex in the absence and presence of the analyte, respectively, [M] is the concentration of the analyte, and K_{SV} is the quenching constant, which reflects the quenching degree of the quencher to the fluorescence intensity of the complex.

Figure 7d–f are the linear fitting curves between different concentrations of Fe^{3+} and the relative fluorescence intensities I_0/I of complexes **1**–**3**. The curve shows that within a certain range, there was a good linear correlation between the ratio of Fe^{3+} concentration and the relative fluorescence intensities of complexes **1**–**3** , and the R^2 and K_{SV} values were $R^2 = 0.9882$, $R^2 = 0.9974$, and $R^2 = 0.9864$ and $K_{SV} = 2.48 \times 10^4\ M^{-1}$, $K_{SV} = 1.99 \times 10^5\ M^{-1}$, and $K_{SV} = 2.524 \times 10^5\ M^{-1}$, respectively. The detection limits of complexes **1**–**3** for Fe^{3+} were calculated to be 0.76, 0.657, and 0.11 μM, respectively, based on the equation LOD = 3δ/slope.

The lower detection limits of these complexes compared to that of MOF sensors for Fe^{3+} detection already reported in the literature indicate that complexes **1**–**3** have better detection performance for Fe^{3+} (Tables S3).

3.4.2.1. Discussion on the Quenching Mechanism. On this basis, the detection mechanism of complexes for Fe^{3+} was further investigated. First, as shown in Figure S4a–c, the simulated PXRD peaks of the complexes before and after Fe^{3+} detection matched well with those of the actual test, which confirmed the integrity of the framework after detection and excluded the fluorescence burst caused by framework collapse. Second, as shown in Figure S4d–f, the IR spectra of the complexes before and after ion identification remain consistent, indicating that no interaction between the detectors and the complexes occurred. As shown in Figure S4g–i, there is a large overlap between the excitation spectrum of the complex and the UV–vis absorption spectrum of the detector. Therefore, the main reason for the fluorescence burst of the complex by Fe^{3+} is the energy competition absorption between the two.

3.4.3. Sensing of Complexes to Anions. Next, we explored the fluorescence recognition ability of the complexes for anions. The experiment process is the same as that in the 3.4.2 section, except that $M(NO_3)_X$ is replaced by K_yX (X = CO_3^{2-}, Cl^-, MnO_4^-, I^-, $Cr_2O_7^{2-}$, $H_2PO_4^-$, HCO_3^- CrO_4^{2-}, PO_4^{3-}, and Br^-). As shown in Figure 8a–c, after adding $Cr_2O_7^{2-}$ and MnO_4^-, the fluorescence intensity of the complexes is obviously weakened. Among them, the fluorescence intensities of **1** and **3** decrease the most significantly after adding MnO_4^- and the decrease in fluorescence intensity of **2** is the most obvious after adding $Cr_2O_7^{2-}$, which indicates that complexes **1** and **3** can be used as ideal fluorescent sensors to selectively detect MnO_4^- and complex **2** can sense $Cr_2O_7^{2-}$. To evaluate the selectivity of the sensing system, the fluorescence responses of MOF and MOF@X (X = $Cr_2O_7^{2-}$ and MnO_4^-) complexes in the presence of different interfering substances were recorded. From the graph of Figure 8g–i, $Cr_2O_7^{2-}$ and MnO_4^- (2 mL, 1.0×10^{-3} mol L^{-1}) can significantly quench the fluorescence of the corresponding complexes, while other

https://doi.org/10.1021/acsomega.1c07351
ACS Omega 2022, 7, 18276−18291

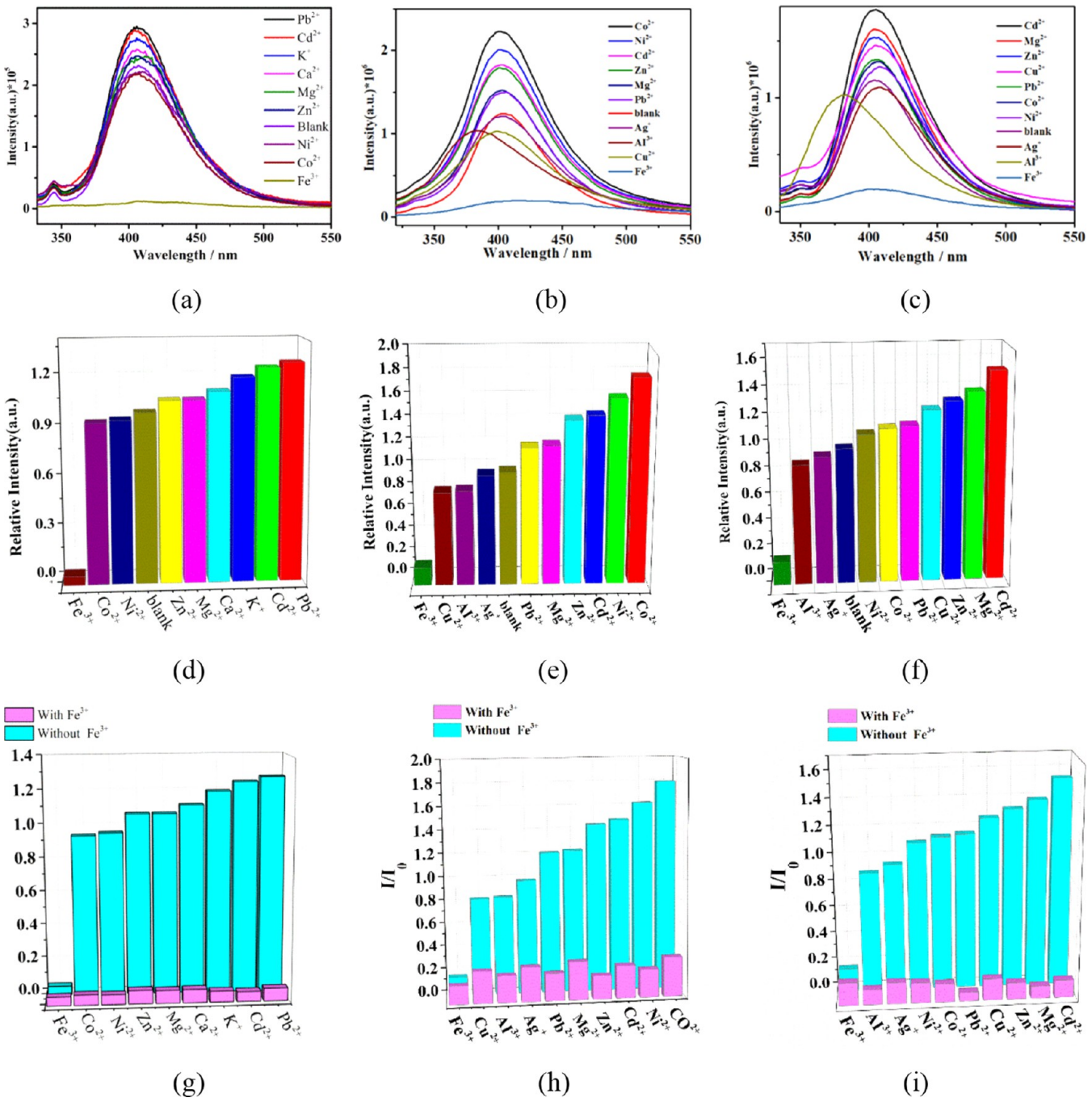

Figure 6. Fluorescence emission spectra of complexes in different metal cation solutions: (a) complex **1**; (b) complex **2**; and (c) complex **3**. Relative fluorescence intensity of complexes in different metal cation solutions: (d) complex **1**; (e) complex **2**; and (f) complex **3**. Relative fluorescence intensity of Fe^{3+} mixed with different metal cations: (g) complex **1**; (h) complex **2**; and (i) complex **3**.

metal ions have less effect on the fluorescence quenching of the complexes. In addition, it can also be observed that the metal ions that may cause interference do not affect the "off" process of complex fluorescence induced by $Cr_2O_7^{2-}$ and MnO_4^-, which indicates that the complexes are more selective for the recognition of $Cr_2O_7^{2-}$ and MnO_4^- than of other metal ions.

The detection sensitivity of the complexes to MnO_4^- and $Cr_2O_7^{2-}$ can be evaluated via fluorescence titration experiments. As shown in Figure 9a–c, the fluorescence intensity of the complex suspensions showed a decreasing trend with the increase of MnO_4^- and $Cr_2O_7^{2-}$ ion concentrations. The fluorescence quenching efficiency of the complex can be quantitatively described according to the SV equation: $I_0/I = 1 + K_{SV}[Q]$.[22] As shown in Figure 9d–f, the fluorescence intensity of the complexes and the concentration curves of MnO_4^- and $Cr_2O_7^{2-}$ show a good linear relationship within a certain concentration range ($R^2 = 0.9844$, $R^2 = 0.9998$, and $R^2 = 0.9963$, respectively). Through the analysis of the SV equation, we obtain the fluorescence quenching constants ($K_{SV} = 1.98 \times 10^4$, 3.704×10^4, and 1.213×10^4 M^{-1}, respectively). At the same time, the calculated detection limits are 0.96, 0.035, and 0.098 μM, respectively. Compared with those of MOF sensors for MnO_4^- and $Cr_2O_7^{2-}$ detection that have been reported in the literature, the detection limit of this

https://doi.org/10.1021/acsomega.1c07351
ACS Omega 2022, 7, 18276−18291

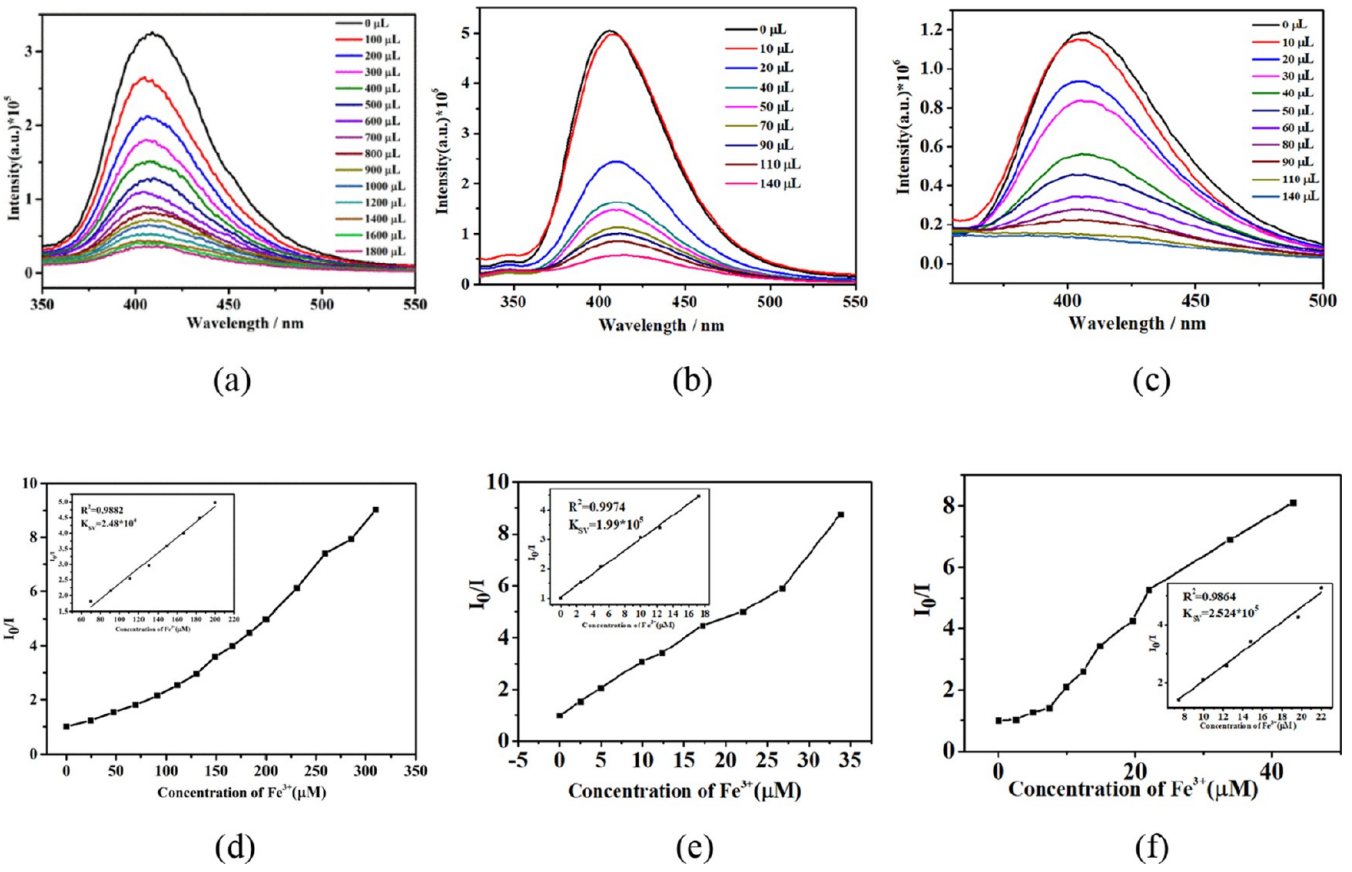

Figure 7. Fluorescence intensity of complexes at different Fe^{3+} concentrations: (a) complex **1**; (b) complex **2**; and (c) complex **3**. Fluorescence intensity I_0/I fitting curves for different concentrations of Fe^{3+} and complexes (SV equation): (d) complex **1**; (e) complex **2**; and (f) complex **3**.

complex is lower, which indicates that complexes **1**−**3** have better detection performance for the corresponding ions (Tables S4 and S5).

3.4.3.1. Discussion on the Quenching Mechanism. As shown in Figure S5a−c, first, the PXRD simulated peaks of the complexes before and after ion detection matched well with the actual tested peaks, which confirmed the integrity of the framework after detection and ruled out fluorescence quenching caused by the collapse of the framework. Second, through IR spectrogram analysis, we observed that the IR spectrum of complex **1** after ion recognition was basically the same as that of the blank group, which ruled out the possibility of interaction between the host and guest (Figure S5d−f). However, the IR peaks of complexes **2** and **3** at about 1690 cm^{-1} disappeared after the ions were identified, which was mainly due to the acid−base coordination effect between the carboxylic acid oxygen atom and Cr(VI) in the complex. Figure S5g−h shows the excitation spectrum of the complex and the UV−vis absorption spectrum of the corresponding detection substance. It is observed that the spectra of the two have a large overlap, which indicates that there is an energy competition absorption effect between the complex and the detection substance. The detection substance absorbs the excitation energy of the complex, so the fluorescence of the complex is quenched.

3.4.4. Sensing of Complexes to Amino Acids. Using the same method as ion exploration, the detection ability of complex amino acids was explored. We have selected 10 amino acids: lysine (Lys), phenylalanine (Phe), isoleucine (Ile), methionine (Met), threonine (Thr), valine (Val), leucine (Leu), histidine (His), tryptophan (Try), serine (Ser), and L-arginine (Arg). As shown in Figure 10a−c, most amino acids have a slight enhancement effect on the fluorescence intensity of complex **1**. Among them, Val has the most obvious enhancement effect on the fluorescence of complex **1**, which is 2.4 times stronger than that of the blank group (Figure 10d), which shows that complex **1** can be used as an excellent sensor for selective detection of Val. However, it is clearly observed that the fluorescence intensity of complexes **2** and **3** can be significantly enhanced by Try solution, which is about 2.47 and 3.8 times higher than that of the complexes in aqueous solution, respectively, while several other amino acids also slightly enhanced the fluorescence intensity of complexes **2** and **3**, but the effect was not significant. In addition, it can also be observed that the emission peak of complex **2** has an obvious blue shift compared with that of the blank group after the addition of Try solution, which indicates that there is an interaction between Try and complex **2** (Figure 10b), and this may be caused by the special interaction between Try and the complex, which indicates that complexes **2** and **3** can be used as excellent sensors for the detection of Try.

In order to explore the sensitivity of the complexes as a sensor to detect Try and Val, a sensitivity test experiment was performed. As shown in Figure 11a−c, the fluorescence intensities of complexes show a gradual increasing trend with the increase of the concentration of Val and Try solutions, and within a certain range, there is a good linear relationship between the concentration of Try and the fluorescence intensity of the complexes, and the linear correlation coefficients, R^2 = 0.9899, R^2 = 0.9900, and R^2 = 0.9878,

https://doi.org/10.1021/acsomega.1c07351
ACS Omega 2022, 7, 18276−18291

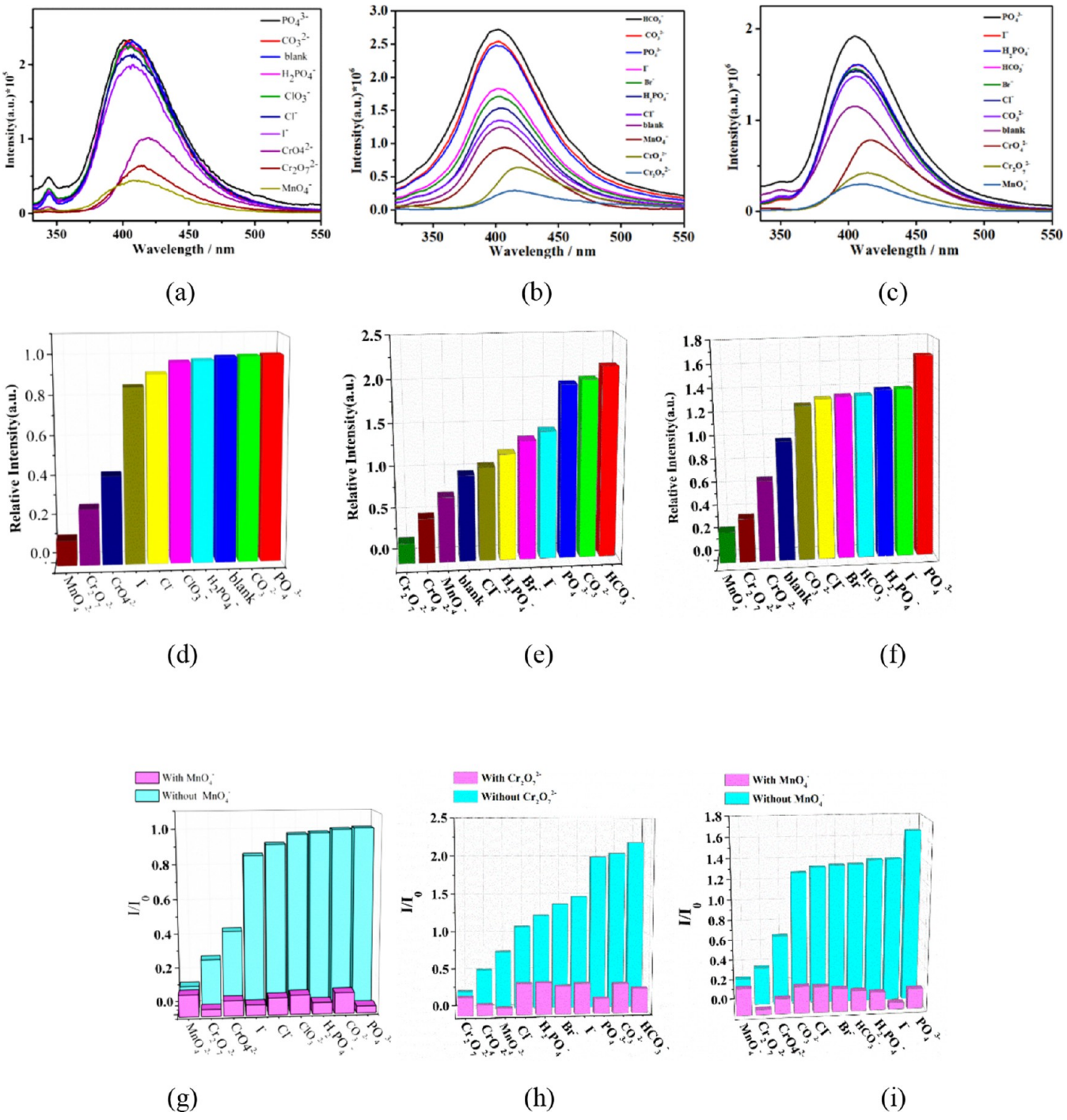

Figure 8. Fluorescence emission spectra of complexes in different metal anionic solutions: (a) complex **1**; (b) complex **2**; and (c) complex **3**. Relative fluorescence intensity of complexes in different metal anionic solutions: (d) complex **1**; (e) complex **2**; and (f) complex **3**. Relative fluorescence intensity of MnO_4^- and $Cr_2O_7^{2-}$ mixed with different anionic solutions: (g) complex **1**; (h) complex **2**; and (i) complex **3**.

respectively, and the linear equations, $y = 1280x + 1.015$, $y = 2000x + 10.7225$, and $y = 11{,}300x + 2.3438$ can be used to express the relationship between the fluorescence intensity I of the complex and the concentration of Try/Val (Figure 11d–f). According to LOD = 3δ/slope, the detection limits of Try/Val for the corresponding complexes are as low as 5.72, 0.065, and 0.249 μM, respectively, which is much lower than the level of Try in human serum (52.9 ± 1.8 μM[25]). Therefore, complexes **2** and **3** can be used as a probe material for detecting Try content. Compared with those of MOF sensors reported in the literature for amino acid detection, the detection limits of complexes **2** and **3** are lower, indicating that complexes **2** and **3** have better detection performance for Try (Table S4).

3.4.4.1. Discussion on the Quenching Mechanism. In order to elucidate the effect of amino acids on the corresponding complexes, the mechanism was explored. The Val amino acid has a slight enhancement effect on the fluorescence intensity of complex **1**. According to reports in the related literature,[26] it may be the energy competition between H_2O and Val around the metal center, and the

https://doi.org/10.1021/acsomega.1c07351
ACS Omega 2022, 7, 18276−18291

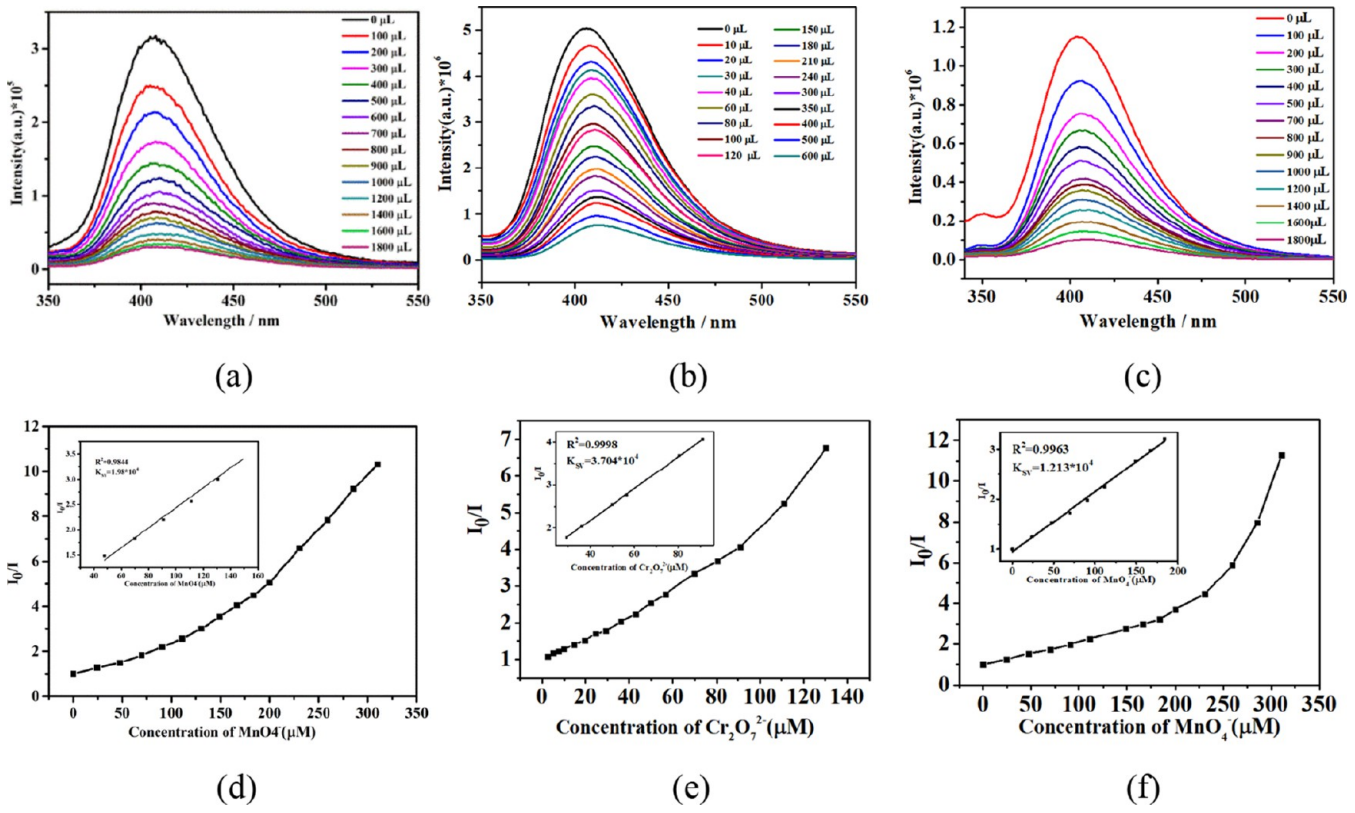

Figure 9. Fluorescence intensity of complexes under different $MnO_4^-/Cr_2O_7^{2-}$ concentrations: (a) complex **1**; (b) complex **2**; and (C) complex **3**; Fluorescence intensity I_0/I fitting curve of complexes with different concentrations of MnO_4^- solution (SV equation): (d) complex **1**; (e) complex **2**; and (f) complex **3**.

electronic interaction between Val and the ligand makes the metal center the surrounding water molecules are reduced, thereby weakening the −OH vibration and resulting in the enhancement of the fluorescence of complex **1**. On the other hand, the Val molecule contains amino groups that can accept protons and the carboxyl group in the complex can give protons, and thus, the two can have acid−base interaction. The weakening of the IR peak at 3447 cm^{-1} in Figure S6d can be verified. As shown in Figure S6e, complex **2** soaked with Try has a sharp emission at 3412 cm^{-1}, which is the stretching vibration peak of the N−H bond in the amine group, which indicates that there is also an interaction between complex **2** and Try. As shown in Figure S6f, the IR peak of complex **3** soaked in Try at 1635 cm^{-1} basically disappears, which also indicates that there is an interaction between the two. Combining the PXRD and UV absorption spectra of the three complexes (Figure S6a−c,g−i), it is concluded that the fluorescence enhancement of complex **1** is mainly caused by the intermolecular interaction, and the main reasons for the fluorescence enhancement of complexes **2** and **3** are the intermolecular interaction and energy competition absorption.

3.4.5. Sensing of Complexes to Antibiotics. Using the same method as the detection of amino acids, the fluorescence recognition ability of the complexes to antibiotics was explored. We chose 11 antibiotics: tinidazole (TNZ), dimetridazole (DMZ), sulfamethoxazole (SMZ), metronidazole (MNZ), ofloxacin (OFX), amoxicillin trihydrate (AMX), tetracycline hydrochloride (TC), chloramphenicol (CAP), sulfadiazine (SDZ), isoniazid (INH), and roxithromycin (RXM). As shown in Figure 12a−c, compared with the blank group, AMX can significantly enhance the fluorescence intensity of the three complexes. TC has the most obvious quenching effect on the fluorescence intensity of these three complexes, and the quenching percentages are about 97, 96, and 98%, respectively (Figure 12d−f). In addition, it was observed that the addition of OFX caused the characteristic emission peaks of the three complexes to undergo a red shift phenomenon, which may be due to the interaction between OFX and the complexes.

Since the fluorescence quenching efficiency of the complex is the highest in the TC solution, the sensitivity of the complex to detect TC was explored with TC as the representative. As shown in Figure 13a−c, the fluorescence intensity of the three complexes gradually decreased with the increase of TC concentration. According to the SV equation, the fluorescence quenching efficiency of complexes **1**, **2**, and **3** on TC can be calculated quantitatively using the following: $I_0/I = 1 + K_{SV}[Q]$.[22] The fluorescence quenching constants of the three complexes are calculated to be 6.87×10^4, 8.5×10^5, and 8.72×10^4 M^{-1}, respectively (Figure 13d−f); the detection limits are determined to be 0.28, 0.154, and 0.32 μM, respectively. Compared with those of MOF sensors for TC detection reported in the literature, the detection limit of these complexes is lower, indicating that complexes **1**−**3** have better detection performance for TC (Table S7).

3.4.5.1. Discussion on the Quenching Mechanism. First, as shown in Figure S7a−c, the PXRD simulated peaks of the complexes before and after TC detection match well with the actual tested peaks, which confirms the integrity of the framework after TC detection and excludes the fluorescence quenching caused by the collapse of the framework.

https://doi.org/10.1021/acsomega.1c07351
ACS Omega 2022, 7, 18276−18291

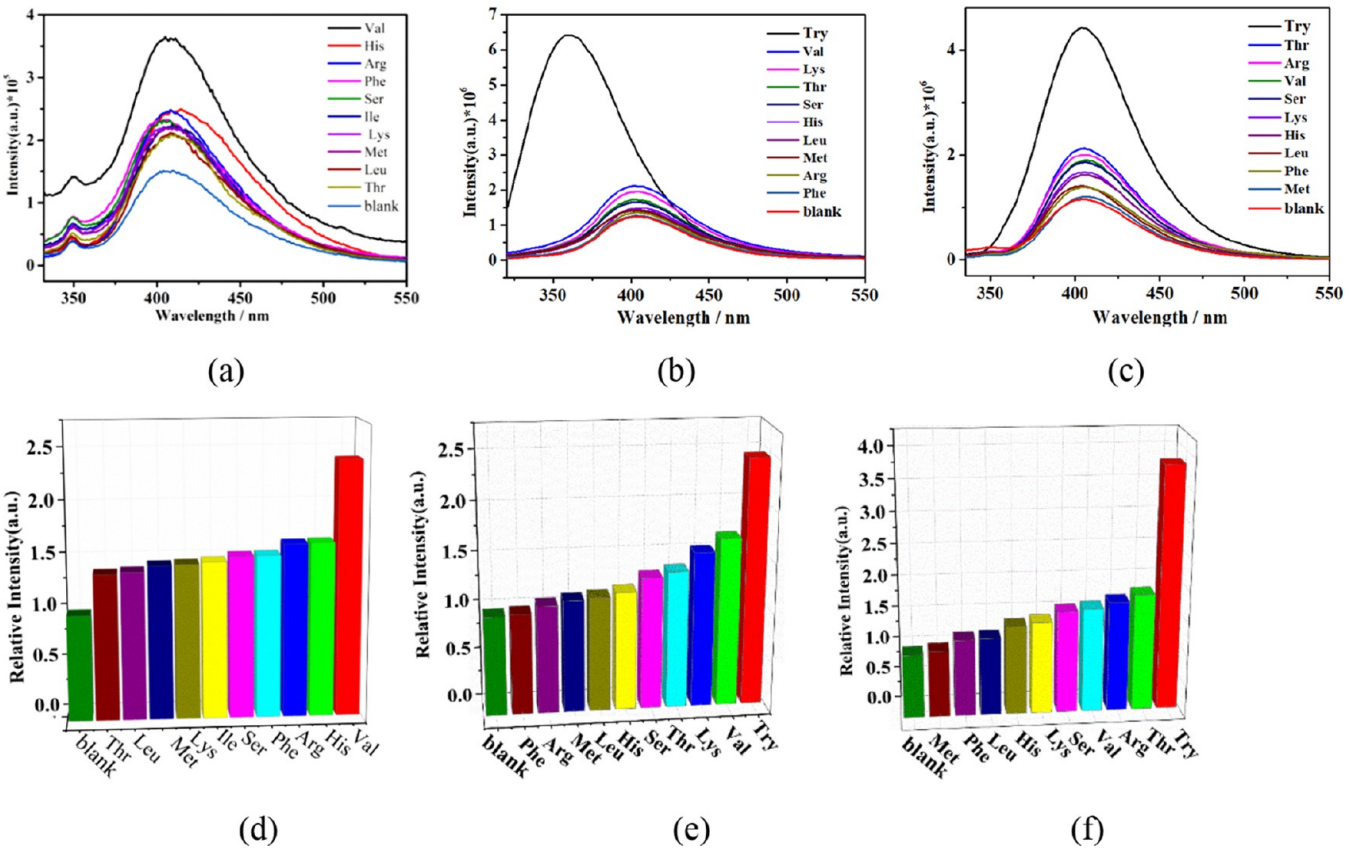

Figure 10. Fluorescence emission spectra of complexes in different amino acid solutions: (a) complex **1**; (b) complex **2**; and (c) complex **3**. Relative fluorescence intensity of complexes in different amino acid solutions: (d) complex **1**; (e) complex **2**; and (f) complex **3**.

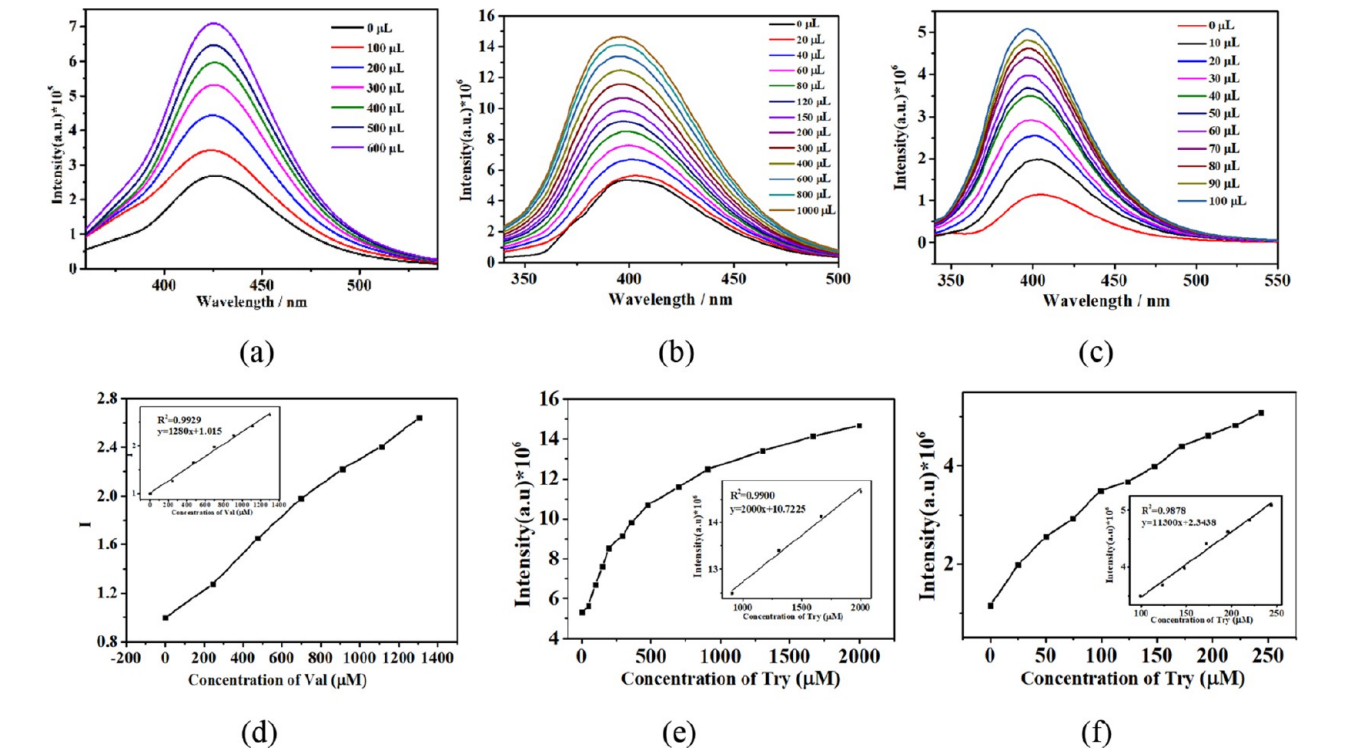

Figure 11. (a) Fluorescence emission spectra of complex **1** in different concentrations of Val solution; (b,c) fluorescence emission spectra of complexes **2** and **3** in different concentrations of Try solution; (d) fitting curve of fluorescence intensity I of complex **1** with different concentrations of Val; and (e,f) fitting curve of fluorescence intensity I of complexes **2** and **3** with different concentrations of Try.

https://doi.org/10.1021/acsomega.1c07351
ACS Omega 2022, 7, 18276−18291

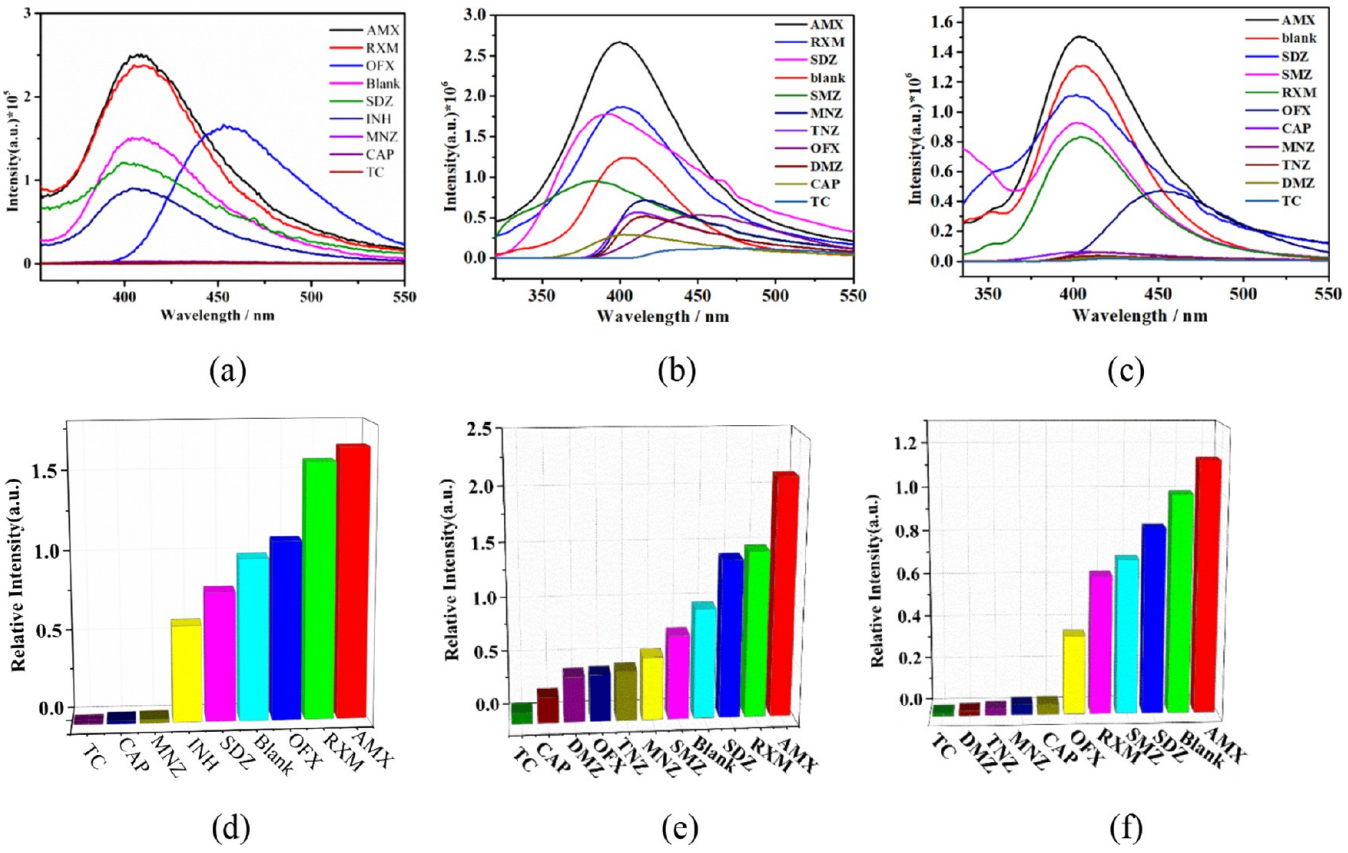

Figure 12. Fluorescence emission spectra of complexes in different antibiotic solutions: (a) complex **1**; (b) complex **2**; and (c) complex **3**. Relative fluorescence intensity of in antibiotic solutions: (d) complex **1**; € complex **2**; and (f) complex **3**.

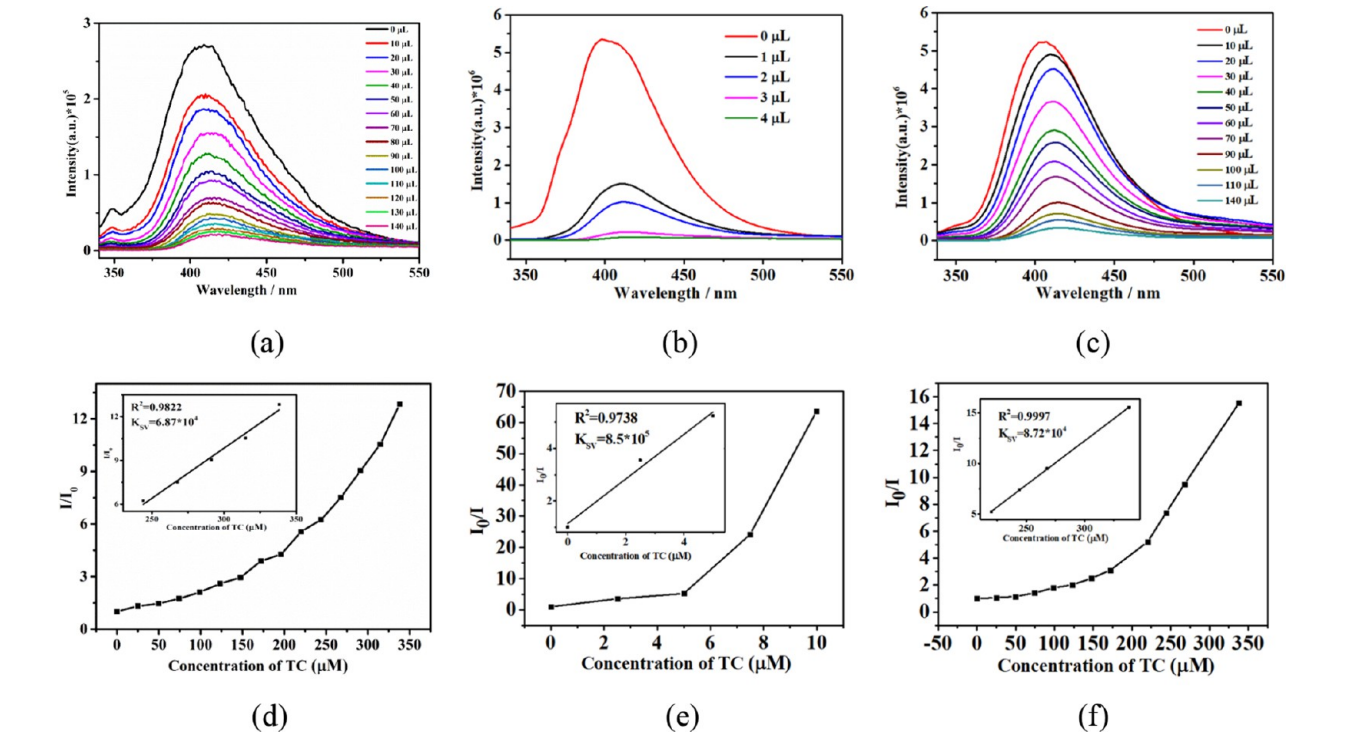

Figure 13. Fluorescence emission spectra of complexes in different concentrations of TC solution: (a) complex **1**; (b) complex **2**; and (c) complex **3**. Fluorescence intensity I_0/I fitting curves of complexes with different concentrations of TC solution (SV equation): (d) complex **1**; (e) complex **2**; and (f) complex **3**.

https://doi.org/10.1021/acsomega.1c07351
ACS Omega 2022, 7, 18276−18291

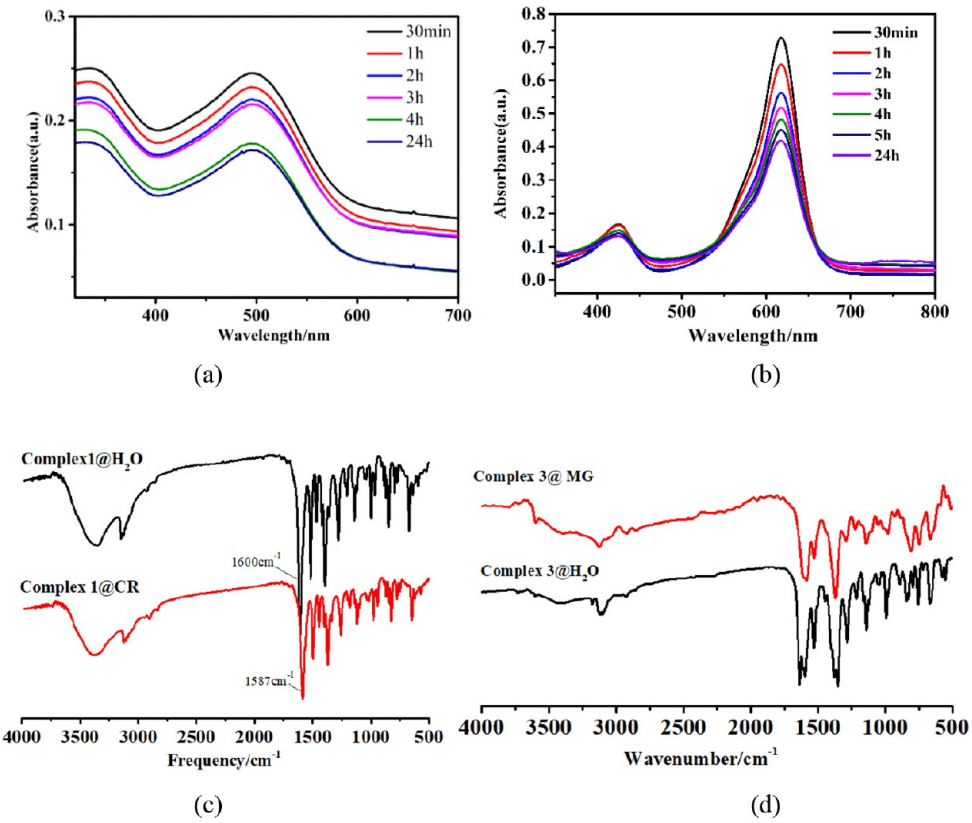

Figure 14. (a) Adsorption behavior of complex **1** toward CR dye; (b) adsorption behavior of complex **3** toward MG dye; (c) IR spectra of complex **1** before and after dye adsorption; and (d) IR spectra of complex **3** before and after dye adsorption.

Second, the IR spectra before and after the detection are analyzed. As shown in Figure S7d−f, the IR peaks of complex **1** show basically no changes, while the IR spectra of complexes **2** and **3** show peak disappearance and shift. The IR peaks of complex **2** shifted from the original 1605, 1569, and 1395^{-} to 1689^{-}, 1611^{-}, and 1431 cm^{-1}, respectively, indicating that there is an interaction between complex **2** and the analyte. Compared with that of the blank group, the IR spectra of complex **3** before and after TC detection almost disappeared at 1635 cm^{-1}, indicating that there is also an interaction between complex **3** and the analyte.

Finally, as shown in Figure S7g−i, the excitation spectrum of the complex and the UV−vis absorption spectrum of the antibiotic have a large overlap, indicating that there is energy competition absorption between the complexes and the detector. Therefore, the fluorescence quenching mechanism of the complexes is mainly attributed to the interaction between the complexes and antibiotic TC and the energy competition absorption between them.

3.5. Dye Adsorption Properties of Complexes 1, 2, and 3. Based on the pore structure of the complexes, their application in the adsorption of organic dyes was studied. We chose nine common dyes used in real life: methylene blue (MEB), bromocresol green (BCG), MO, Congo red (CR), brilliant cresol blue (BCB), neutral red (NR), saffron red T (ST), crystal violet (CV), and rhodamine 6G (R6G). 5 mg of the complex powder was added to 4 mL of a dye solution with a concentration of 1 ppm (10^{-6} mol/L). After sonication for 30 min, it was left for 24 h in the dark. To obtain the absorption degree of the complex to the dye, the formula $(A_0 - A_t)/A_0 \times 100$ (where A_0 is the absorbance of the dye without the complex and A_t is the absorbance of the complex to the dye at any time) is used to calculate the adsorption efficiency of the complex to the dye. As shown in Figure S8, only complex **1** exhibits a certain adsorption capacity for CR dyes, and its adsorption efficiency is 41.64%, but there is no obvious adsorption for other dyes. The adsorption efficiency of complex **2** on organic dyes is shown in Figure S9. Among them, it has an adsorption effect on BCB, R6G, ST, and MEB. The adsorption efficiencies are 4.17, 17.6, 18.6, and 12.5%, respectively, but there is almost no adsorption effect on other dyes. As shown in Figure S10, complex **3** only showed a relatively obvious adsorption effect on MG, and its adsorption efficiency was 65%, while it had almost no adsorption effect on other dyes. Subsequently, the adsorption sensitivity detection of complexes **1** and **2** to the corresponding dyes at different times was explored. As shown in Figure 14a,b, the longer the soaking time is, the greater the adsorption capacity of the complexes to dyes, and when it reaches 24 h, the adsorption capacity almost tends to be stable and remains unchanged. Furthermore, we explored the adsorption mechanism of CR by complex **1**, as shown in Figure 14c, and after dye adsorption, the stretching vibration peak of C═O in the carboxyl group of complex **1** at 1600 cm^{-1} is shifted to 1587 cm^{-1}, which is mainly due to the uncoordinated carboxylic acid group in complex **1** and the amino group in the CR dye molecule forming a hydrogen bond, so the adsorption mechanism is attributed to the interaction between complex **1** and CR. As shown in Figure 14d, the stretching vibration peak of −C═O in the carboxyl group of complex **3** at 1638 cm^{-1} disappeared after dye adsorption, which may be due to the weak interaction between complex **3** and MG. Therefore, the adsorption of MG

https://doi.org/10.1021/acsomega.1c07351
ACS Omega 2022, 7, 18276−18291

by complex **3** is mainly attributed to its porous structure and weak interaction.

4. CONCLUSIONS

In conclusion, three novel MOFs were successfully synthesized in this paper. All three synthesized complexes can be used as excellent sensors to selectively detect Fe^{3+} and TC through the quenching effect. Complexes **1** and **3** can detect MnO_4^- via a fluorescence-off process, and complexes **2** and **3** can detect Try via a fluorescence-on process. The dye adsorption experiment revealed that complex **1** has a certain adsorption capacity for CR dye, and complex **3** has an adsorption effect on MEB dye. The adsorption mechanism is mainly attributed to the porous structure of the complexes and the weak interaction between the complexes and the dye molecules.

■ ASSOCIATED CONTENT

Supporting Information

The Supporting Information is available free of charge at https://pubs.acs.org/doi/10.1021/acsomega.1c07351.

Crystallographic data, geometric parameters of the structures, PXRD patterns, IR spectra, TGA curves, and dye adsorption curve measurements (PDF)

■ AUTHOR INFORMATION

Corresponding Authors

Yunxia Yang − *Key Laboratory of Eco-environment-related Polymer Materials, Ministry of Education, College of Chemistry and Chemical Engineering, Northwest Normal University, Lanzhou 730070, China*; Email: yangyx80@163.com

Xiangxiang Wu − *Scientific Research and Experiment Center, Henan University of Chinese Medicine, Zhengzhou 450046, China*; Email: wuxx-415@126.com

Authors

Yingwa Guo − *Key Laboratory of Eco-environment-related Polymer Materials, Ministry of Education, College of Chemistry and Chemical Engineering, Northwest Normal University, Lanzhou 730070, China*

Shiying Xia − *Key Laboratory of Eco-environment-related Polymer Materials, Ministry of Education, College of Chemistry and Chemical Engineering, Northwest Normal University, Lanzhou 730070, China*

Xiaona Ma − *Key Laboratory of Eco-environment-related Polymer Materials, Ministry of Education, College of Chemistry and Chemical Engineering, Northwest Normal University, Lanzhou 730070, China*

Complete contact information is available at: https://pubs.acs.org/10.1021/acsomega.1c07351

Notes

The authors declare no competing financial interest.

■ ACKNOWLEDGMENTS

This project was sponsored by the Henan Science Fund for Excellent Young Scholars (212300410057), Henan Scientific and technological Innovation Talents Project (20HAS-TIT050), and Henan Scientific Research Funding Project for Overseas Staffs 2020 (no: 29).

■ REFERENCES

(1) Kitagawa, S. Metal-organic frameworks (MOFs). *Chem. Soc. Rev.* **2014**, *43*, 5415−5418.

(2) Jie, H.; Jialiang, X.; Jiacheng, Y.; Na, L.; Xianhe, Bu. Recent Advances in Luminescent Metal-Organic Frameworks for Chemical Sensors. *Sci. China Mater.* **2019**, *62*, 1655−1678.

(3) Yang, X.; Ma, L.-F.; Yan, D. Facile Synthesis of 1D Organic-Inorganic Perovskite Micro-Belts with High Water Stability for Sensing and Photonic Applications. *Chem. Sci.* **2019**, *10*, 4567−4572.

(4) Li, J.; Jiang, L.; Chen, S.; Kirchon, A.; Li, B.; Li, Y.; Zhou, H.-C. Metal-Organic Framework Containing Planar Metal-Binding Sites: Efficiently and Cost-Effectively Enhancing the Kinetic Separation of C_2H_2/C_2H_4. *J. Am. Chem. Soc.* **2019**, *141*, 3807−3811.

(5) Wang, X.-N.; Zhang, P.; Kirchon, A.; Li, J.-L.; Chen, W.-M.; Zhao, Y.-M.; Li, B.; Zhou, H.-C. Crystallographic Visualization of Postsynthetic Nickel Clusters into Metal-Organic Framework. *J. Am. Chem. Soc.* **2019**, *141*, 13654−13663.

(6) Jrad, A.; Abu Tarboush, B. J.; Hmadeh, M.; Ahmad, M. Tuning Acidity in Zirconium-Based Metal Organic Frameworks Catalysts for Enhanced Production of Butyl Butyrate. *Appl. Catal., A* **2019**, *570*, 31−41.

(7) Horcajada, P.; Gref, R.; Baati, T.; Allan, P. K.; Maurin, G.; Couvreur, P.; Férey, G.; Morris, R. E.; Serre, C. Metal-Organic Frameworks in Biomedicine. *Chem. Rev.* **2012**, *112*, 1232−1268.

(8) Wang, H. Y.; Ge, J. Y.; Hua, C.; Jiao, C. Q.; Wu, Y.; Leong, C. F.; D'Alessandro, D. M.; Liu, T.; Zuo, J. L. Photo-and Electronically Switchable Spin-Crossover Iron (II) Metal-Organic Frameworks Based on a Tetrathiafulvalene Ligand. *Angew. Chem., Int. Ed.* **2017**, *56*, 5465−5470.

(9) Zorlu, Y.; Erbahar, D.; Çetinkaya, A.; Bulut, A.; Erkal, T. S.; Yazaydin, A. O.; Beckmann, J.; Yücesan, G. A cobalt arylphosphonate MOF-superior stability, sorption and magnetism[J]. *Chem. Commun.* **2019**, *55*, 3053−3056.

(10) Liu, W.; Li, N. n.; Zhang, X.; Zhao, Y.; Zong, Z.; Wu, R.; Tong, J.; Bi, C.; Shao, F.; Fan, Y. Four Zn (II)-MOFs as Highly Sensitive Chemical Sensor for the Rapid Detection of Tetracycline, o-Nitro Phenol, $Cr_2O_7^{2-}/PO_4^{3-}$, Fe^{3+}/Al^{3+} in Water Environment[J]. *Cryst. Growth Des.* **2021**, *21*, 5558−5572.

(11) Liu, S.; Xiang, Z.; Hu, Z.; Zheng, X.; Cao, D. Zeolitic imidazolate framework-8 as a luminescent material for the sensing of metal ions and small molecules. *J. Mater. Chem.* **2011**, *21*, 6649−6653.

(12) Singha, D. K.; Majee, P.; Mondal, S. K. Visible detection of explosive nitroaromatics facilitated by a large stokes shift of luminescence using europium and terbium doped yttrium based MOFs. *RSC Adv.* **2015**, *5*, 102076−102084.

(13) Jiang, H.-L.; Feng, D.; Wang, K.; Gu, Z.-Y.; Wei, Z.; Chen, Y.-P.; Zhou, H.-C. An exceptionally stable, porphyrinic Zr metal-organic framework exhibiting pH-dependent fluorescence. *J. Am. Chem. Soc.* **2013**, *135*, 13934−13938.

(14) Chen, Y.-Z.; Jiang, H.-L. Porphyrinic metal-organic framework catalyzed heck-reaction: fluorescence "turn-on" sensing of Cu (II) ion. *Chem. Mater.* **2016**, *28*, 6698−6704.

(15) Yi, F.-Y.; Chen, D.; Wu, M.-K.; Han, L.; Jiang, H.-L. Chemical sensors based on metal-organic frameworks. *ChemPlusChem* **2016**, *81*, 675−690.

(16) Ding, B.; Liu, Y.-Y.; Huang, Y.-Q.; Shi, W.; Cheng, P.; Liao, D.-Z.; Yan, S.-P. Structural variations influenced by ligand conformation and counteranions in copper (ii) complexes with flexible bis-triazole ligand. *Cryst. Growth Des.* **2008**, *9*, 593−601.

(17) Liu, L.; Zhang, H.-Y.; Wang, Y.-M.; Wang, H.-J.; Chen, S.; Sun, J.-W. Synthesis and characterization of a new (1D+1D) polyoxometalate-based polypseudo-rotaxane coordination polymer. *J. Solid State Chem.* **2019**, *277*, 779−785.

(18) Blatov, V. A. Nanocluster analysis of intermetallic structures with the program package TOPOS. *Struct. Chem.* **2012**, *23*, 955−963.

(19) Chen, S.-S.; Liu, Q.; Zhao, Y.; Qiao, R.; Sheng, L.-Q.; Liu, Z.-D.; Yang, S.; Song, C.-F. New metal-organic frameworks constructed from the 4-imidazole-carboxylate ligand: structural diversities,

luminescence, and gas adsorption properties. *Cryst. Growth Des.* **2014**, *14*, 3727−3741.
(20) Yao, S.-L.; Xu, H.; Zheng, T.-F.; Liu, S.-J.; Chen, J.-L.; Wen, H.-R. Rare Fluorescence Red-Shifted Metal-Organic Framework Sensor for Methylamine Derived from an N-Donor Ligand. *Cryst. Growth Des.* **2021**, *21*, 5765−5772.
(21) Khatua, S.; Goswami, S.; Biswas, S.; Tomar, K.; Jena, H. S.; Konar, S. Stable multiresponsive luminescent MOF for colorimetric detection of small molecules in selective and reversible manner. *Chem. Maters.* **2015**, *27*, 5349−5360.
(22) Sahoo, S. K.; Sharma, D.; Bera, R. K.; Crisponi, G.; Callan, J. F. Iron(III) selective molecular and supramolecular fluorescent probes. *Chem. Soc. Rev.* **2012**, *41*, 7195−7227.
(23) Dutta, B.; Jana, R.; Bhanja, A. K.; Ray, P. P.; Sinha, C.; Mir, M. H. Supramolecular aggregate of Cadmium(II)-based one-dimensional coordination polymer for device fabrication and sensor application. *Inorg. Chem.* **2019**, *58*, 2686−2694.
(24) Zhu, S.-Y.; Yan, B. A novel covalent post-synthetically modified MOF hybrid as a sensitive and selective fluorescent probe for Al^{3+} detection in aqueous media. *Dalton Trans.* **2018**, *47*, 1674−1681.
(25) Matysik-Woźniak, A.; Paduch, R.; Turski, W. A.; Maciejewski, R.; Jünemann, A. G.; Rejdak, R. Effects of tryptophan, kynurenine and kynurenic acid exerted on human reconstructed corneal epithelium in vitro. *Pharmacol. Rep.* **2017**, *69*, 722−729.
(26) Zheng, K.; Liu, Z.-Q.; Huang, Y.; Chen, F.; Zeng, C.-H.; Zhong, S.; Ng, S. W. Highly luminescent Ln-MOFs based on 1, 3-adamantanediacetic acid as bifunctional sensor. *Sens. Actuators, B* **2018**, *257*, 705−713.

https://doi.org/10.1021/acsomega.1c07351
ACS Omega 2022, 7, 18276−18291